Event Screening for the Chandra X-Ray Observatory High Resolution Camera (HRC)

Stephen S. Murray*, Jon Chappell, Almus Kenter, Mike Juda, Ralph Kraft, Martin Zombeck, Gary Meehan, Gerald Austin, and Jack Gomes

Harvard-Smithsonian Center for Astrophysics
60 Garden Street
Cambridge, MA 02138

Abstract

The Chandra X-ray Observatory High Resolution Camera is an improved version of similar Microchannel Plate (MCP) based detectors that were previously used on the *Einstein* and ROSAT X-ray observatories. The HRC consists of two detectors in a common housing, and sharing some processing electronics. Only one detector operates at a time. The HRC-I is a $100mm \times 100mm$ device that is used for wide field of view imaging with sub-arcsecond angular resolution. The HRC-S is a $300mm \times 30mm$ device that is used to readout the Low Energy Transmission Grating Spectrometer (LETGS) providing very high spectral resolution. The main differences from previous missions are the larger format MCP's, radioisotope free MCP glass, and an active Cosmic Ray anti-coincidence shield. Event processing in the HRC is limited to digitizing selected signals from the readout device and transmitting these to the ground. As a result, it is possible to examine and screen the data during processing. Algorithms have been developed to identify non-X-ray events thereby reducing the detector background. Event screening can also detect and filter out "bad" events that might otherwise degrade image quality.

Keywords: X-Ray Detector, MCP, Digital Processing

1 Introduction

The High Resolution Camera [1] on the Chandra X-ray Observatory [2] is an advanced version of the imaging X-ray detectors (HRI's) that were successfully flown and operated on the *Einstein* Observatory (1978-1981) [3]and the ROSAT Observatory (1990 - 1999) [4]. The X-ray sensor is a CSI coated Microchannel Plate (MCP) which is the top plate of a chevron pair. The MCP's provide an electron gain of $\sim 2 \times 10^7$producing an electron charge cloud that is sensed by a readout consisting of two orthogonal planes of wires (the Crossed Grid Charge Detector CGCD). The grid wires are 0.0081 inches apart, and they are connected to each other with thin film resistors. Every 8^{th} wire is attached to an external charge sensitive amplifier (tap). There are two detectors in the Camera, one (the HRC-I) is a $100mm \times 100mm$ device optimized for direct imaging in the focus of the Chandra Telescope. The second, the HRC-S, is a strip of three $100mm \times 30mm$ MCP's in a single holder that is optimized for reading out a dispersive Low Energy Transmission Grating Spectrometer (LETGS) [7]. A total of 128 low power hybrid charge sensitive amplifiers are used for the HRC. Figure 1 shows a schematic view of the HRC, and illustrates the fine position charge division technique that is described below.

*Further author information: E-mail: ssm@head-cfa.harvard.edu

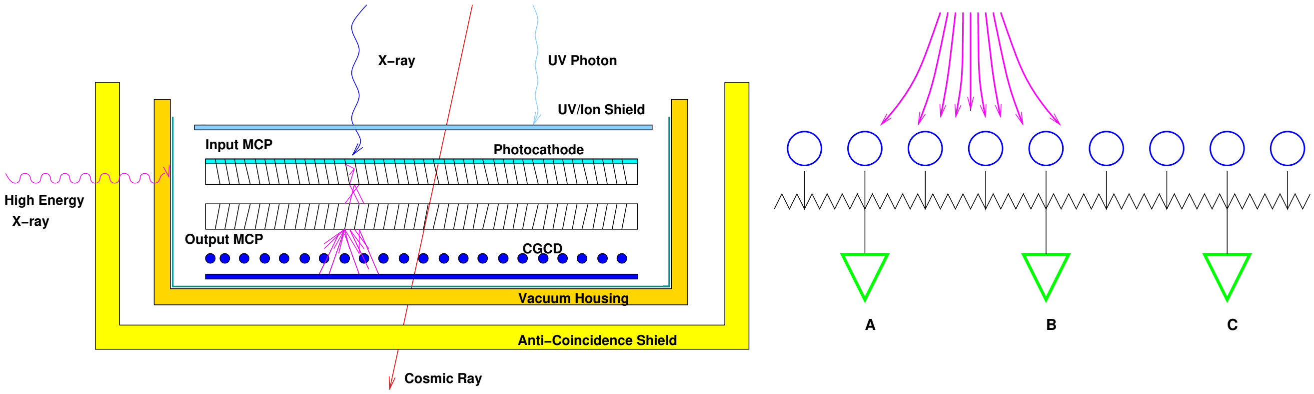

Figure 1: Schematic view of the HRC shows the major elements of the detector. The MCP chevron is contained in a vacuum housing that is surrounded by a five sided plastic scintillator for Cosmic Ray reject. On the right an exploded view of one plane of the Crossed Grid Charge Detector readout is illustrated. The wires are connected by discrete resistors with readout amplifiers (taps) every eighth wire.

The MCP's for HRC are made with low noise glass [8] [9] [10], i.e., radioisotope have been minimized, in order to reduce the internal background rate to extremely low levels. For HRC-S the MCP's were provided by Philips Photonics, and for HRC-I the MCP's were manufactured by Galileo Electro Optics Corporation (now Burle). The typical background rates achieved in the laboratory are less than $0.1\,ct\,cm^{-2}sec^{-1}$. Chandra was placed in an elliptical high earth orbit with 10,000 km perigee and 140,000 km apogee. In this orbit the ambient Cosmic Ray background is higher than for lower equatorial orbits that stay below the Earth's radiation belts. At the time of launch the Cosmic Ray flux was $\sim 2-3\,ct\,cm^{-2}sec^{-1}$. In order to deal with this source of background, an active plastic scintillator anti-coincidence shield surrounds the HRC housing. A veto signal from the shield is used to identify events triggered by Cosmic Rays. Depending on the mode of operation, processing for these events is terminated (normal mode), or the events are flagged in the telemetry with a veto bit for later ground reject.

In the case of the HRC-I, the active Cosmic Ray rejection reduces the non-X-ray background from about $250\,ct\,sec^{-1}$ to about $50\,ct\,sec^{-1}$[11]. For HRC-S, a timing error in the event processing sequencer renders the anti-coincidence ineffective leading to significantly higher background than desired. Fortunately, the detailed event data that is included in the telemetry allows post-facto event screening based on the charge and pulse height distributions. Using the screening techniques described below, background rejection for HRC-I approaches the pre-launch expected value. For HRC-S, event screening reduces background by about a factor of two to three depending on location in the detector (energy in the dispersed spectrum from LETGS).

2 Event Position Calculation

2.1 Coarse-Fine Charge Division

The HRC uses a coarse-fine position readout [12] [13] where the coarse event position is estimated from the readout tap with the largest signal, and the fine position is a charge division calculation using the neighboring three amplifiers at the coarse location. An event is detected by a signal taken from the output electrode of the MCP chevron stack. This is a fast signal that initiates a firmware sequencer in the HRC electronics. Each of the CGCD amplifier fast and slow signals are examined in the event processing electronics. The fast signals are used to estimate the event coarse position, and the slow signals associated with that coarse position are routed to ADC's where their amplitudes are digitized for transmission to the ground. The two planes of the CGCD are treated independently giving the two orthogonal position coordinates (U and V) of the event.

The fine position calculation (illustrated in Figure 1) for the HRC uses the Ohmic properties of the Crossed Grid Charge Detector (CGCD) and assumes that the input impedance of the readout amplifiers is small compared to the wire-to-wire resistance along the grid. Event positions are determined in a coarse-fine algorithm that permits extension to arbitrarily large detectors (needed for the HRC on Chandra). The coarse position is determined by identifying which amplifiers along the readout are triggered, and taking the average location of these coarsely space readout taps as the initial estimated position. Four amplifier signals around the estimated coarse position are routed to the fine position processor. The peak signal from the central two amplifiers is determined, and if necessary the coarse position is adjusted from its initial estimate. Only the peak amplifier and its nearest neighbors are digitized. Thus, the event data that is entered in the telemetry consists(for each coordinate axis) of the location of the central amplifier and the three digitized (12 bit) values of the central signals for that location.

During ground processing, the fine position component is calculated using the charge division among the central three amplifier taps (A, B, C) resulting in an interpolation accurate to about 1/2% of the distance between amplifiers. The fine position is given by

$$f_p = \frac{C - A}{A + B + C} \tag{1}$$

where f_p ranges from -1/2 to +1/2 as the event location varies from halfway between taps A and B to halfway between taps B and C. The total event position is then given by:

$$t_p = p_{tap}(c_p + f_p + 1/2) \tag{2}$$

where p_{tap} is the number of pixels per tap (256), and c_p is the coarse position, i.e., the tap number of the B amplifier (starting at 0). The extra 1/2 tap term, fixes the origin of the position readout at the center of the first amplifier tap.[1] For the HRC, the amplifier spacing is $1.64592mm$, with the fine position digitized to 256 pixels per tap, this corresponds to $6.429375\mu m$ per pixel.[2]

2.2 Gaps and De-gapping

There is an expected correction to the calculated fine event positions due to the "charge spill-over" effect [12], where some of the total signal is not included in the three amplifiers which therefore biases the charge division calculation. This is the fundamental reason for the presence of "gaps" in the raw data images. These are not truly gaps in the sense that there are missing parts of an image. The gaps are due to event positions being miscalculated (relative to a perfect readout) with the result that certain positions are not populated and certain other positions appear to be overpopulated.

The removal of these "gaps" is the process called de-gapping. It involves a transformation from the raw calculated fine position of an event to its correct position had there not been any loss of collected charge. Simulations and studies of the details of the charge collection on a CGCD [13] show that the corrections can be approximated by a low order polynomial expression of the form:

$$f_c = af_p + bf_p^2 + cf_p^3 + ... \tag{3}$$

where f_p is the raw fine position of an event as given by Equation 1. The coefficients are denoted as the first, second, third,... order terms of the de-gap. The de-gap coefficients can be estimated on a global basis or as a function of coarse position. For the Chandra HRC the de-gapping coefficients were derived from a combination of pre-launch calibration data using flat fields of illumination, and post-launch calibration data taken when the HRC was out of the focus position and viewing a radioactive calibration source (Fe^{55}). The de-gapping was done independently for the U and V axes of the detector, but as a function of the coarse position in each axis [5] [6].

[1] No real events can actually have a total position of 0 when defined in this manner.

[2] This pixel size was chosen to slighly oversample the actual spatial resolution of the HRC which has been measured to be $20\mu m$ FWHM.

3 Simulations

3.1 Gaps versus Charge Cloud

The HRC readout can be simulated in one dimension by integrating the charge from a modeled electron charge cloud distribution falling on a grid of equally spaced conductors (wires), which are resistively connected, and applying Ohm's law to calculate the charge collected on the readout amplifiers. Previous measurements have shown that the charge cloud is symmetric and has a "core-halo" shape [13]. A good approximation to the charge cloud is the sum of a Gaussian and Lorentzian distribution that have a common origin and roughly equal peak amplitudes. Using the tap spacing as the unit of distance, the simulations show good agreement with the HRC-I when the Gaussian and Lorentzian sigma and gamma respectively are about 0.25 of a tap. These are set as the nominal values for the plots shown below. The narrow case has these parameters set to 0.10 tap, and the wide case 0.40 tap.

A useful representation of the simulations has been a plot of the event fine position calculated using Equation 1 versus the true position. An example is shown in Figure 2, where three simulations with varying charge cloud widths are plotted. This plot clearly shows the "gaps" as missing calculated locations near ± 0.5 and their dependence on the charge cloud width. When the charge cloud is narrow compared with the tap spacing there is no spill over effect and no gap. With a wide charge cloud, spill over is significant and the gaps are large. The nominal cloud width values approximately simulate the gap sizes that are seen in the HRC-I

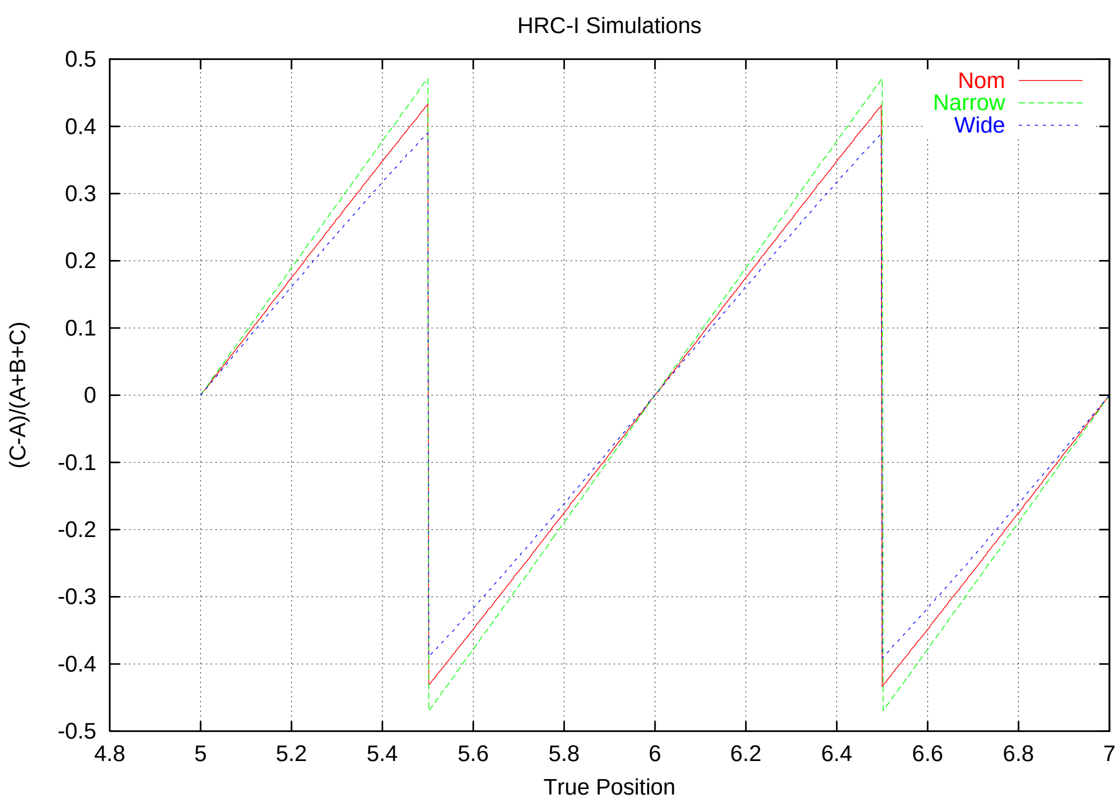

Figure 2: Simulations of uncorrected fine position versus true position for HRC-I with varying charge cloud width. The narrow charge cloud produces little spill over and the gaps are small. The wide charge cloud results in larger gaps.

3.2 An Alternative View of the Data

Another useful representation (which does not depend in knowing the true fine event position) is a plot of the calculated fine position versus the normalized central tap amplitude,

$$f_b = B/(A+B+C) \tag{4}$$

For the same simulations shown in Figure 2, the plots of $f_p\, vs\, f_b$ are shown in Figure 3. The effects of the size of the charge cloud are much more apparent in these plots which illustrates the sensitivity of the relationship to the electron cloud shape.

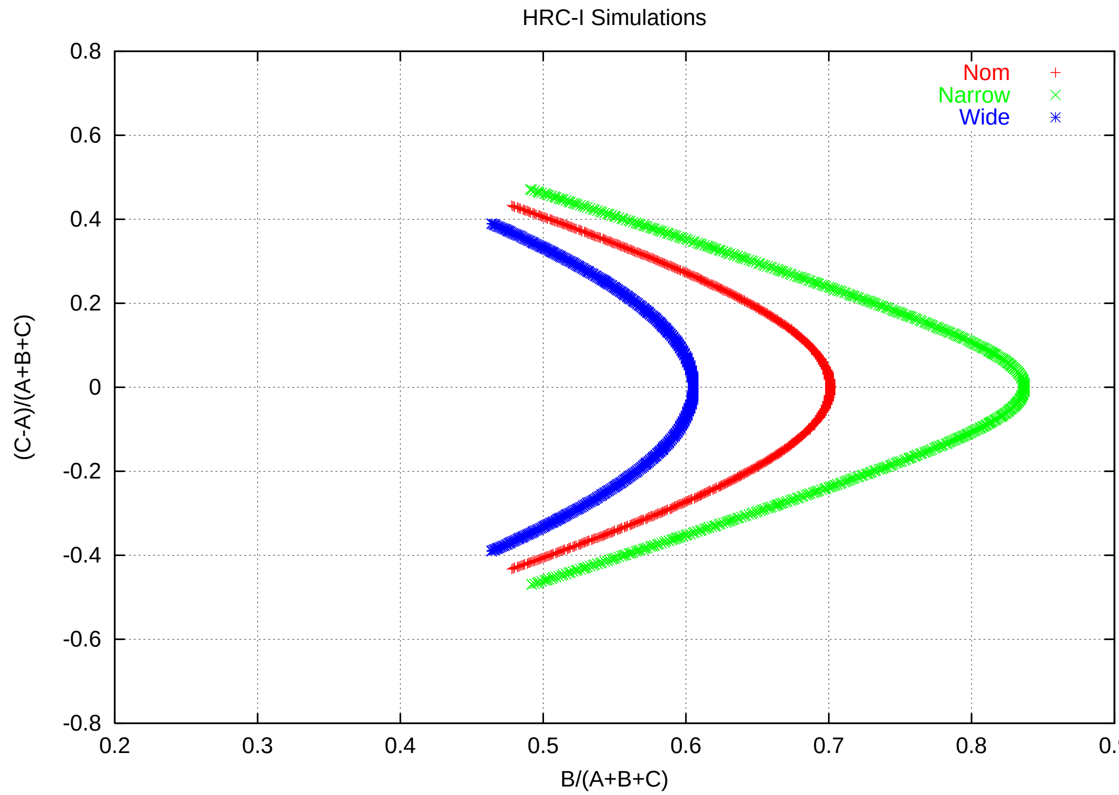

Figure 3: Simulations of the uncorrected fine position versus the normalized central tap amplitude for HRC-I for various charge cloud widths.

Inspection of the plots in Figure 3 suggests that the relationship between f_p and f_b might be approximated by a hyperbolic function of the standard form:

$$\frac{(f_b - h)^2}{a^2} - \frac{f_p^2}{b^2} = 1 \tag{5}$$

where h is the offset from the origin of the center of the hyperbola, and $(h - a)$ is the location of the "nose" of the hyperbola on the f_b axis. The asymptotic slope of the hyperbola is given by $m = b/a$. Solving for f_p we get:

$$f_p = b\sqrt{\frac{(f_b - h)^2}{a^2} - 1} \tag{6}$$

A least squares fit of this function to the nominal simulation case gives an excellent fit with parameter values shown below. A plot of the fitted function overlays the simulated data so well that the curves are indistinguishable as seen in Figure 4

The hyperbolic function that approximates the relation between the simulated quantities has not be derived algebraically and may not be absolutely exact. However, simulations show that the hyperbolic approximation is quite good over a wide range of parameters for the electron charge cloud distribution, which is the physical quantity that

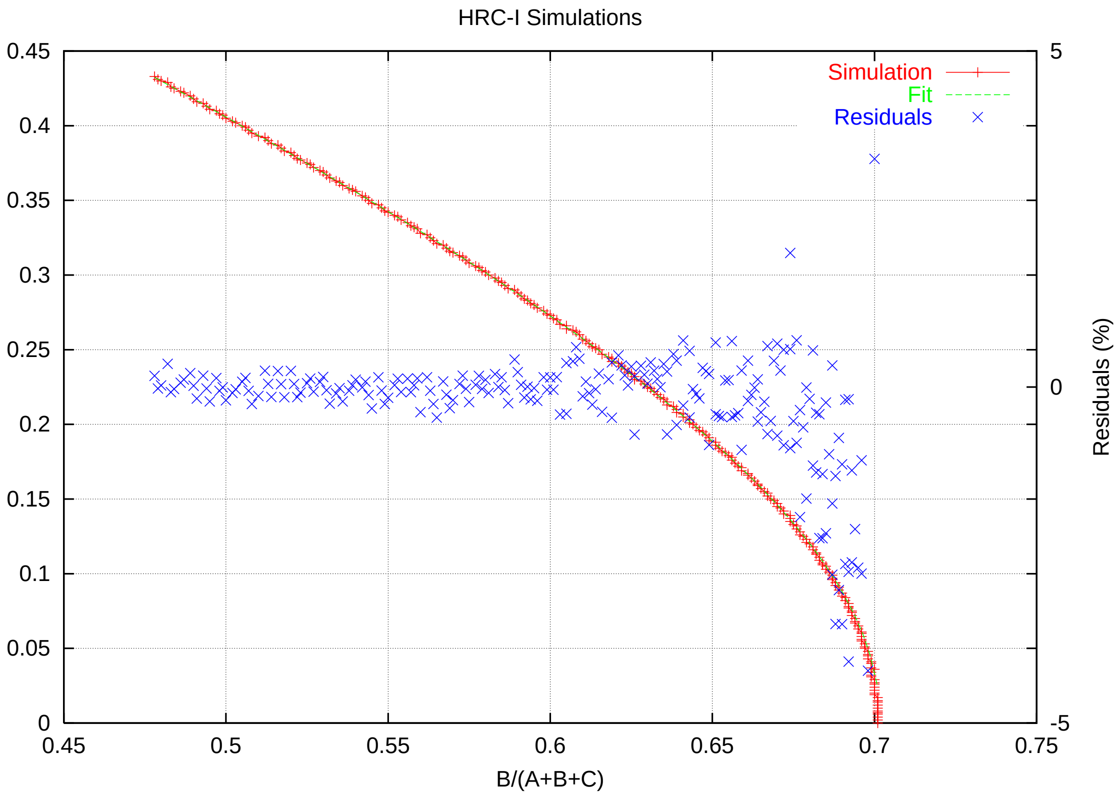

Figure 4: Fit of hyperbolic function to the simulated HRC. The best fit parameter values are a=0.3353(0.3720), b=0.3263(0.3454), h=1.0364(1.0738). The two curves are virtually identical. Also shown are the residuals between the simulated data and the best fit hyperbola.

characterizes the detector readout. Work is in progress to determine the sensitivity and quality of the hyperbolic fit, and to find the proper relation between the fitting parameters and the values of the parameters of the simulated charge cloud: the widths and relative contribution of Gaussian and Lorentzian components.

4 Flight Data

4.1 The f_p, f_b Plane

Examination of pre-launch and flight data show that as predicted from the simulations, there is a strong correlation of the observable quantities f_p and f_b. This is shown in Figure 5 where data from the HRC-I on-orbit calibration source (taken in August 1999) is used. In Figure 5 the HRC-I U-axis data are plotted. The data include background events that were not rejected by the veto shield, internal MCP background events, and events from the Fe^{55} calibration source. As seen in the figure, the events cluster strongly along a locus of positions with scattered events that fill in the enclosed space and extend to the left. Events that do not lie near to the locus tend to have identifiable abnormalities. The low values of f_b indicate events where the coarse position is wrong and thus amplifiers with no real signal were selected for processing. For some events the "flatness" is often high (i.e., the ratio C/B and A/B both exceed 0.5) typical of wide events that are produced by Cosmic Rays at oblique angles. Many events outside the locus have more than one readout amplifier with a pulse height greater than 3600 digital units (DU). This is a symptom of highly saturated events where the MCP signal is large enough to exceed the dynamic range of the tap amplifiers. The plot also shows that the locus for $f_p > 0$ is tighter than for negative values. This is due to a systematic electronic ringing that is described in another paper being presented at this conference [14] and so will not be discussed further here.

The characteristics observed in Figure 5 are typical, with similar results for the HRC-I V-axis, and the HRC-S U and

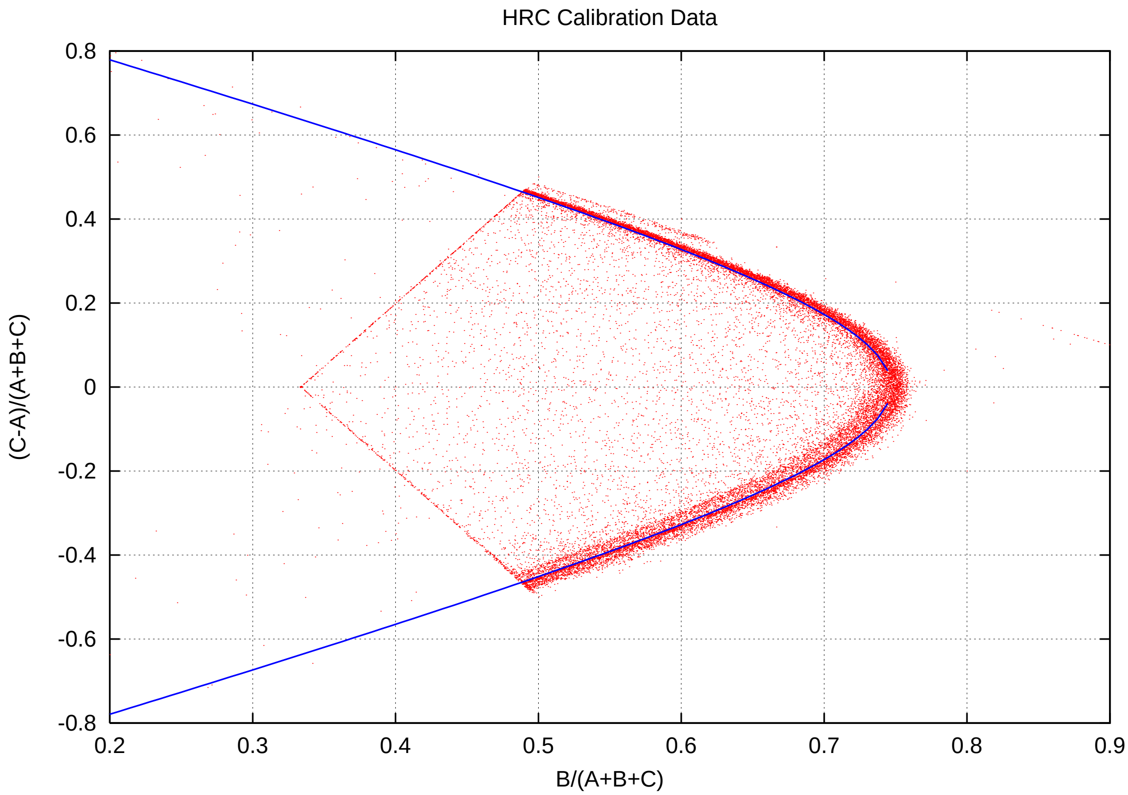

Figure 5: An f_p, f_b plot for the HRC-I from data obtained during on-orbit calibration source observation. Also shown is the best fit hyperbolic function for these data, using the parameters listed in Table 1

V axes. Only the detailed shapes of the curves that characterize the locus of valid events are different as indicated in more detail in Table 1below.

4.2 Hyperbolic Fits

Following the same procedure used for the simulated data, we find that the fine position (f_p) is well fit as a function of the normalized peak amplifier signal (f_b). The hyperbolic function of Equation 6 gives a very good fit to the observed $(f_p,\ f_b)$ distribution. For the Chandra HRC the best fit values of the three parameters (a, b, h) are given in Table 1. Figure 5 also shows the best fit hyperbola, which goes through the dense locus of events and is used to define part of the event screening described in the following section.

Table 1: Hyper-fit Parameters

	HRC-I		HRC-S	
Parameter	U	V	U	V
a	0.3110	0.3050	0.2706	0.2706
b	0.3030	0.2730	0.2620	0.2480
h	1.0580	1.1000	1.0180	1.0710

5 Event Screening

5.1 Screening Tests

As previously discussed, there are several characteristics associated with events that are either not X-rays, or are X-ray events with some distortion. A series of screening tests have been developed to recognize these events and filter them from the data stream. First the event amplitude is checked, If the PHA is less than 20 DU then the event was probably initiated in the second MCP and not from an X-ray. Next the individual tap amplifier amplitudes are checked. If they are all below 20 DU, then the event coarse position was miscalculated and therefore the location is invalid. This type of event is most likely caused by a tracking Cosmic Ray that passes through the MCP at shallow angle. Several sets of tap amplifiers are triggered and the coarse encoder then gives an incorrect central location.

The next standard test looks for the characteristic signature of amplifier saturation at the taps. When an extremely high amplitude event occurs, the three adjacent tap amplifiers exceed their linear dynamic range and produce a voltage that translates to a digitized signal in the telemetry of $>$3600 DU. The “saturation” test checks for all three tap amplifiers exceeding this level. These events are probably not due to X-rays. They are either Cosmic Ray induced, or ion feedback events.

The next screening test, examines the ratio of the off peak tap amplitudes to the peak tap amplitude. For normal X-ray events, the charge distribution is relatively narrow and therefore, at most one of these ratios should exceed 0.5. The “flatness” test excludes events when both ratios are greater than 1/2.

The last screening test, examines the location of an event in f_p, f_b plane as described in the next section. It is by far the test that filters out the most events.

5.2 Zone of Acceptance

Events which do not lie near to the locus described in Figure 5 above are very likely to be non-X-ray events. Flat field calibration data taken at the SAO HRC test facility were examined to help determine the X-ray and non-X-ray distributions of events in the (f_p, f_b) plane. The final pre-launch HRC calibration flat fields were taken with the detector operating at a high data rate, so that the ratio of true X-ray events to background is very high ($>$ 1000). Virtually all events taken in a flat field exposure lie within a small and well defined region of the (f_p, f_b) plane, whereas most of the non-X-ray background events lie outside. The zone of acceptance is the region bounded by the best fit hyperbolic functions given in Table 1 with the parameter h varied by $\pm$0.0300.

The actual in flight performance differs from the ground calibration in that the total HRC event rates are typically 200-300 cts/sec, and most of these are produced by charged particles. For HRC-I, the penetrating cosmic ray component can be identified using the particle shield veto signal (the anti-co signal) which is generated when an energetic charged particle passes through the 5-sided plastic scintillator box that surrounds the HRC housing. For the HRC-S the anti-co signal comes too late relative to the MCP event trigger signal and falls outside of the fixed coincidence timing window, thus rendering the anti-co signal ineffective. Even for the HRC-I the anti-co veto does not fully eliminate all background events. The typical HRC-I valid event rate (after veto) is 40-50 cts/sec, whereas the pre-launch expectation was 10-20 cts/sec. For HRC-S the valid event rate remains in the 200-300 cts/sec range and it is necessary to invoke edge blanking to reduce this rate to a level that does not fill the available telemetry space of $\sim 184\,c/s$.

Figure 6 shows the same data as Figure 5, but with the zone of acceptance described above plotted as two hyperbolas. By excluding events that are not within the zone of acceptance, the non-X-ray background is reduced by about a factor of two, while the X-ray rate remains unchanged (within better than 95%).

While the quality of the fit of a hyperbolic function to the measured f_p versus f_p relation is very good, and also very stable, the fundamental basis for this “ad hoc” functional form has not yet been demonstrated. None-the-less, the operational application of a functional form to the observed correlation is a useful tool that allows for meaningful event filtering and the empirically derived functional form makes the implementation of the screening algorithm simple. With almost one year of operation, there has been no detectable change to the shapes of the zone of avoidance. Additional ground calibration data from approximately two years prior to launch also conform to the

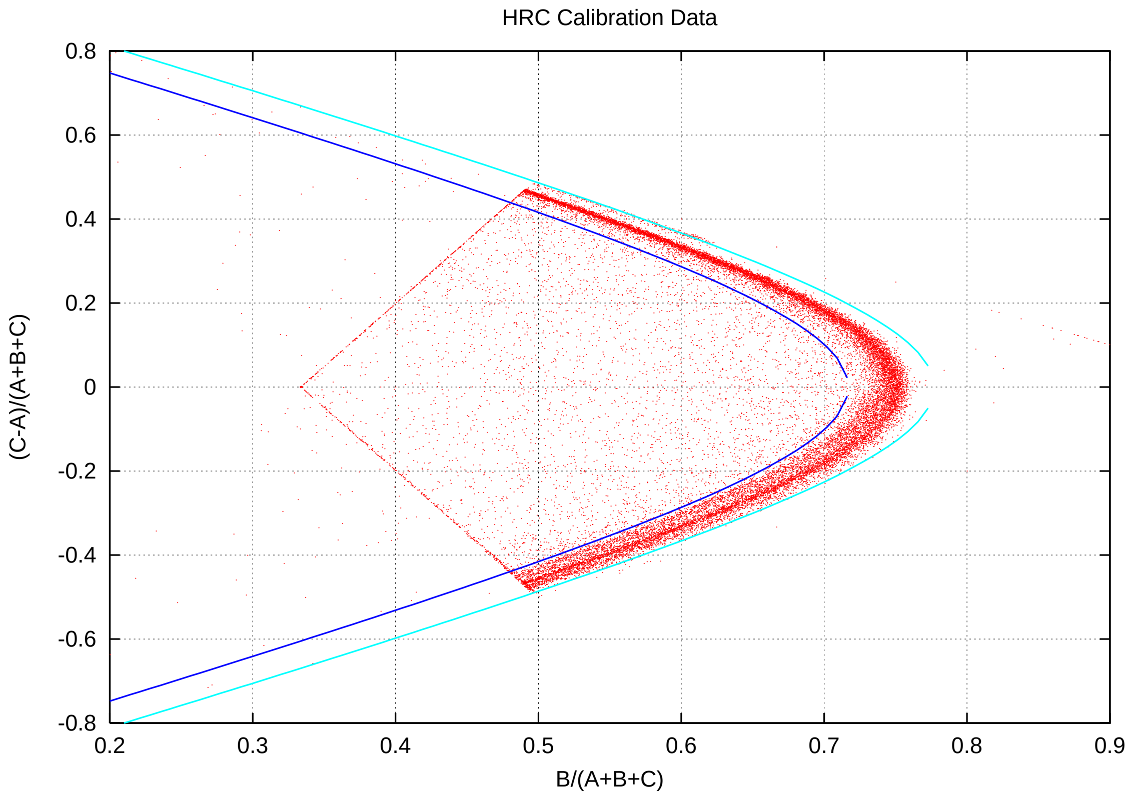

Figure 6: The same data as in Figure 5. Here the boundaries of the zone of acceptance are plotted. They are constructed from the best fit hyperbola to the good event locus offset by ± 0.030 in the f_b axis.

flight generated data. Thus, there is a few year history of stability in the MCP behavior that would indicate that the event screening is robust and reliable.

5.3 Effects of Event Screening

In addition to improving signal to noise by eliminating much more of the non-X-ray background than the real X-ray events, the "hyperbolic" screening algorithm also helps to eliminate other sorts of "bad" events from the data. The most significant of these is the so-called ghost image which occurs when a readout amplifier saturates or is otherwise distorted. An analysis of early flight data shows that this effect which is typically a few percent of all true X-ray events, is completely eliminated (to the level of less than 0.5%).

Figure 7 shows the effect of event screening on an actual HRC-I image. The 15 ksec observation was made in late 1999. Table 2 summarizes the results of the screening process.

Table 2: Summary of Event Screening for Cen-A Observation

Events	Test
685,841	Unfiltered
14,080	Bad Fine Positions (i.e., zero sum)
59,464	PHA $<$ 20 DU
2,228	Amplifier Saturation
808	Flat Distribution
165,098	Out of Zone (Hyperbola Test)
442,521	Remaining after Screening

When the hyperbolic screening test was used on an image of Cen-A (HRC-I) about 35% of all events were rejected from the image. For all of the X-ray sources in that image (except the nucleus and the diffuse galaxy related emission) the loss of events in the source was less than 5% (in many cases consistent with no loss) while the background was decreased by about 35-40%. Inspection of the two images in Figure 7 shows how the “ghost” image from the bright central source (nucleus) is eliminated and the overall background was decreased.

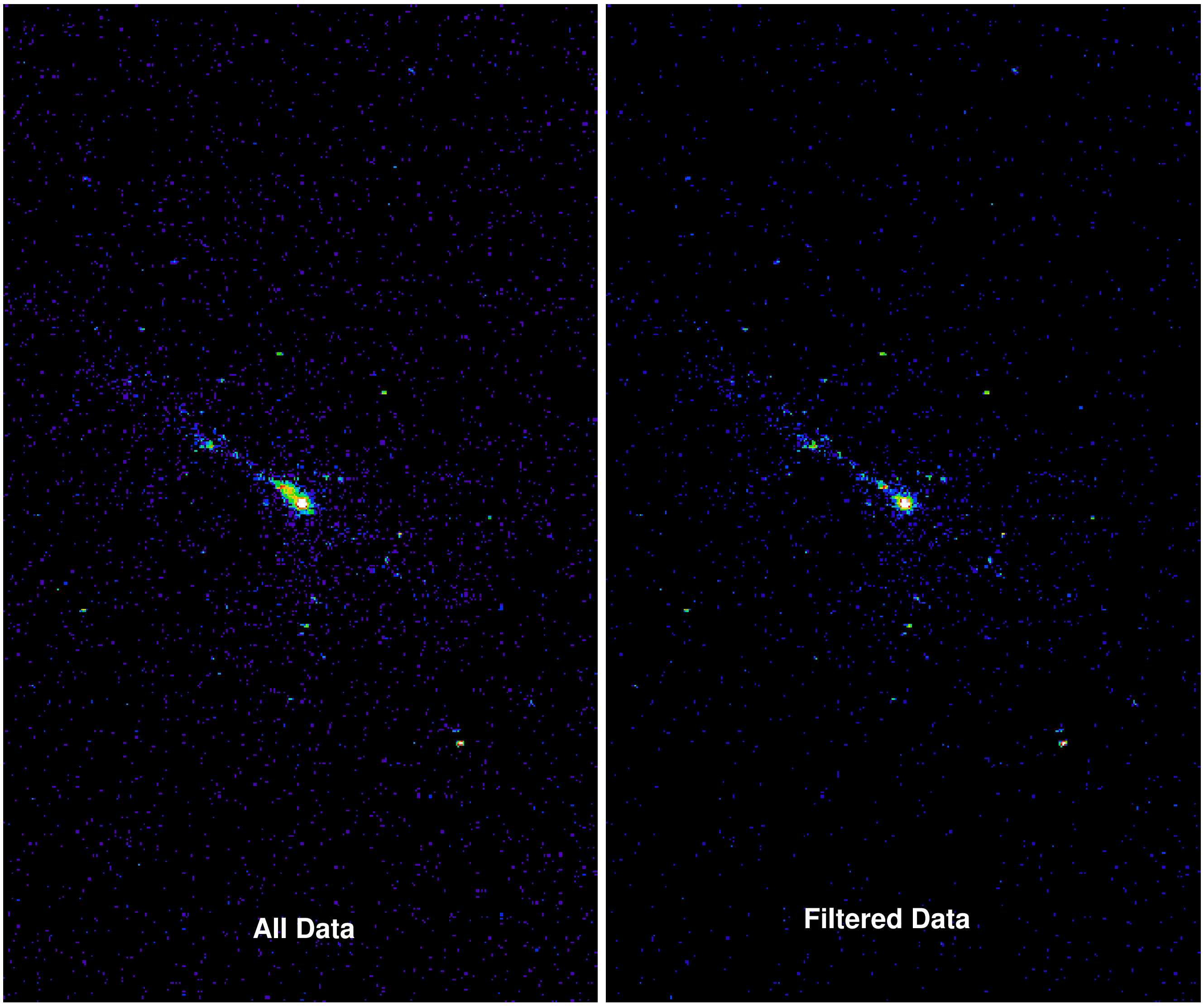

Figure 7: An HRC-I observation of the nearby Active Galaxy Nucleus Centaurus-A (Cen-A) showing the effects of event screening on image quality and background reduction.

6 Conclusions

The detailed event data that are telemetered to the ground provide information that can be used to filter non-X-ray events from the data stream. Some of the screening tests are very simple and involve looking for erroneous coarse position estimates, extreme event amplitudes (both too low or too high), and simple estimates of an event's charge cloud width. While these tests are relevant, they do not produce very large numbers of rejected events.

The most significant event filter is the zone of acceptance test (or hyperbolic test) which tests measurable quantities that describe the details of the electron charge cloud distribution. We find that normal X-rays are described by a very restrictive relationship between the uncorrected fine position (Equation 1) and the normalized central tap amplitude (Equation 4).

When event screening is used, the non-X-ray background is greatly reduced. Typically a factor of two is achieved with almost no loss of valid X-ray events. This background reduction improves the signal to noise in HRC data allowing fainter sources to be detected for a given exposure.

Event screening also reduces mislocated events which improves image quality. The most significant improvement is the elimination of "ghost" images that appear in the HRC-I, where 2-3% of events are mislocated along one detector axis by amounts ranging from a few pixels to almost 100 pixels.

7 Acknowledgments

This work was supported by NASA contracts NAS8-38248 and NAS8-39073. The authors would also like to thank the Chandra X-Ray Center for their operation of the Chandra Observatory and the processing of telemetry that was made available for the analysis used in this work.

References

[1] Murray, S.S., and Chappell, J,H., "The Advanced X-Ray Astrophysics Facility High Resolution Camera", Proc. SPIE 597, 279, 1986

[2] Weisskopf, M.C., O'Dell, S.L., Elsner, R.F., and van Speybroeck, L.P., "Advanced X-Ray Astrophysics Facility (AXAF): an overview", Proc. SPIE 2515, 312, 1995

[3] Giacconi, R. et al. "The Einstein (HEAO 2) X-ray Observatory", Ap.J. 230 540, 1979

[4] Trumper, J. "ROSAT", Sterne und Weltraum 29, 222, 1990

[5] Kenter, K, et al. "In-flight Performance and Calibration of the Chandra High Resolution Camera Imager (HRC-I)", Proc. SPIE 4012, XXX, 2000

[6] Kraft, R. P., et al. "In-flight Performance and Calibration of the Chandra HRC-S Readout" Proc. SPIE 4012, XXX, 2000

[7] Brinkman, A.C., van Rooijen, J.J., Bleekerm J.A.M., Dijkstra, J.H. and Heise, J. "Low Energy X-ray Transmission Grating Spectrometer for AXAF" Proc. SPIE 597, 232, 1986

[8] Garcia, M.R., Chappell, J.H., Murray, S.S., Feller, W.B., and Fraser, G.W. "Low Noise Microchannel Plate Detectors for X-ray Astronomy" Proc. SPIE 1140, 101, 1989

[9] Chappell, J.H., Martin, R.K., Murray, S.S., and Zombeck, M.V. "Background Reduction in Microchannel Plates" Proc. SPIE 1344, 176, 1990

[10] Murray, S.S., et al. "AXAF High Resolution Camera(HRC): Calibration and Recalibration at XRCF and Beyond" Proc. SPIE, 3114, 11, 1997

[11] Murray, S.S., et al. "In-flight Performance of the Chandra High Resolution Camera", Proc. SPIE, 4012, XXX, 2000

[12] Murray, S.S., and Chappell, J.H. "The AXAF High Resolution Camera" Proc. SPIE 982, 48, 1988

[13] Chappell, J.H., and Murray, S.S. "Position Modeling for the AXAF High Resolution Camera (HRC)" Proc. SPIE 1159, 460, 1989

[14] Juda, M. et al. "Improving Chandra High Resolution Camera Event Positions via Corrections to the Crossed Grid Charge Detector Signals" Proc. SPIE 4140, XXX, 2000